26th AIAA Applied Aerodynamics Conference
Aug. 18–21, 2008/Honolulu, Hawaii

CFD Prediction of Rotor Loads using Time-Spectral Method and Exact Fluid-Structure Interface

Seongim Choi *
Department of Mechanical Engineering, Stanford University, Stanford, CA 94305

Anubhav Datta †
Eloret Corporation, Ames Research Center, Moffett Field, CA 94035

The primary objective of this paper is to study time-spectral method for simulating helicopter rotor flows in steady flight. The intent is to compare the accuracy of predicted vibratory loads (both airloads and structural loads) with time-accurate computations and quantify the aliasing error and convergence behavior in a precise manner. The CFD/Comprehensive Analysis coupling method in this paper is different from the state-of-the-art. We implement an exact fluid-structure interface for rotors and formulate a modified delta coupling procedure, that is generic for advanced geometry blades, underlying structural models, and unstructured surface grids. The Counter 8534 flight from the U. S. Army/NASA Airloads Program, the highest vibration flight of this helicopter, is used for validation. The fastest and minimal implementation of the method, with 11 time instances for a 4-bladed rotor, predicts the vibratory normal forces and pitching moments within 5–10% accuracy with respect to time-accurate simulations in about one-fifth the computational time. The largest errors occur in vibratory chord forces (10 to 20%). This level of error generates un-satisfactory levels of error in structural loads. However, the primary source of error is aliasing, which for this flight decreases asymptotically with an increasing number of time instances. We demonstrate an accuracy level of 1% and 0.1% in airloads with 17 and 25 time instances respectively. These correspond to one-third and one-half the computational time of a time-accurate solution. It is concluded that time-spectral method in CFD can be used effectively for the prediction of rotor vibratory loads. However, without any anti-aliasing filter, reliable prediction of structural loads requires a number of time instances at least four times the blade number – still at one-third the time, approximately, compared to a time-accurate solution.

I. INTRODUCTION

Spectral methods have been widely used for the different types of the problems in fluid dynamics that are governed by the partial differential equations with periodic boundary conditions. They can be distinguished by the class of the method (Galerkin, collocation, or tau) or by the type of the trial/basis functions (trigonometric polynomials, Chebychev polynomials and Legendre polynomials).[1]

A time-spectral method in this paper is standard algorithm based on the Fourier collocation method, where the periodic solution at each Fourier node (grid point or time instance in the time domain) is approximated by a discrete Fourier expansion. The key idea of the time-spectral method is to apply the Fourier spectral method to the temporal discretization rather than to the conventional spatial discretization.

A number of engineering problems which involve the unsteady periodic motions have already used time-spectral method, such as the areas of turbomachinery,[2] flapping wing analysis,[3] micro air vehicle, etc. An application of time-spectral method to the helicopter rotor flow analysis has been conducted in our previous

*Research Associate
†Rotorcraft Dynamicist

work[4–6] for the steady-level flight conditions of the UH-60A Black Hawk helicopter - high speed 8534, low speed 8513/8515, and stall case 9017.

The main advantage of the spectral method is high-order accuracy it achieves compared to the finite difference method. A spectral accuracy can be obtained when the number of harmonics larger than Nyquist frequency is included for a solution approximation, and it has proven to be equivalent to the accuracy of the infinite-order finite difference method.[7] With much smaller number of Fourier nodes the method demonstrates higher than or as good accuracy as that of the finite difference mehod.[1]

Another advantage of the spectral method is that Fourier collocation differentiation can be represented by a simple form of matrix (instead of applying FFT both in time and frequency domains). Thus, if the matrix form of Fouier collocation differentiation is applied to the time derivative term in the governing equations, then the formulation becomes periodic steady-state in time domain and the solution procedure becomes independent of time evolution. This fact is appreciated to a large extent in the case of turbomachinery simulation where initial transient time to reach periodic steady-state is considerable, but rotor flows typically take less time to reach periodic steady-state solutions ($\sim$1/4 of a period).

The characteristic related to the steady-state formulation brings the time-spectral method a high potential to be used for a design optimization framework for the unsteady periodic problems. A number of design optimization procedure require sensitivity information of the functionals (or objective functions) and a state-of-the-art gradient computation procedure, such as the adjoint solution method,[9,10] can be enormously cost-intensive in both time and memory for the unsteady problems.[11,12] However, the steady-state formulation of the time-spectral method make the steady adjoint solution formulation leveraged in the unsteady design optimization problems. Although the design optimization is not a focus of the present paper, a research on that aspect is on-going[6] and the current work on the validation of the time-spectral method for the helicopter rotor flow analysis is essential for the reliability of design optimization.

However, since the time-spectral method is based on the Fourier collocation method, it inherently contains the error behaviors of the classical Fourier spectral method; truncation error and aliasing error. The accuracy of the time-spectral method is greatly dependent on the number of Fourier modes we include for a solution approximation. At the same time, the time-spectral method is a global scheme requiring the solutions at all grid points in time during the solution procedure, and the inclusion of larger number of time instances improves the accuracy at a spectral convergence rate, but unavoidably incurs increase in computational expense and thus deteriorate the efficiency of the time-spectral method.

A rigorous study on the effects of the number of time instances on the accuracy, the convergence of the solution, and computational time savings has not been provided and these issues are closely related to the aliasing error behaviors of the time-spectral method.

One of the main purposes of our study is to precisely quantify the amount of aliasing errors in helicopter rotor flow analysis with respect to the varying numbers of time instances and to determine how many number of time instances are necessary to provide an acceptable accuracy at a computational cost less than that of time-accurate method, such as finite-difference method.

This study has a practical importance when it comes to the prediction of the rotor vibratory loads, the dominant frequency content of which typically consists of lower-harmonics, and the application of the time-spectral method makes particularly attractive. However a precise prediction of rotor vibratory loads requires accurate elastic deformation data which are obtained from CFD/CA (Comprehensive Analysis) coupling method through iterative solution procedure.

Our previous time-spectral computation for the rotor flow analysis has been limited to the particular trim conditions which were fixed through the entire simulation with elastic deformations prescribed by the data obtained from else where (the existing data obtained from time-accurate computation based CFD coupled with CA). Thus, the capability of the TS method to couple with a structural or comprehensive analysis code has not been studied in a rigorous sense.

Another purpose of this study is to investigate whether time-spectral method can be used for CFD/CA coupling procedure. The efficiency of TS method can make the coupling process less time consuming than the conventional time accurate computation coupled with CSD codes. The second part of this paper will elaborate the fluid-structure interface implementation using both conventional and exact coupling procedure.

The prediction of vibratory loads in helicopter rotors require, in addition to CFD and CSD, a solution procedure for simultaneously determining the rotor operating state. The operating state is determined by the vehicle flight dynamics (VFD) – trajectory and control pitch angles. A procedure for coupled CFD/CSD/VFD in steady flight was proposed by Tung et al. in 1986.[16] It is widely applied today and is

well-known as *delta* or *loose* coupling procedure. There are no procedures, yet, for unsteady maneuvers. In steady flight, VFD is simple: the trajectory is trivial, and the control angles are determined by the coupled trim condition. The *delta* or *loose* coupling procedure is implied in rotorcraft literature by the frequent use of the term CFD/Comprehensive Analysis. Though used interchangeably with CFD/CSD, it implies an analysis which uses both the CSD and trim models of current comprehensive codes, while replacing its lower order lifting-line (or surface) aerodynamic model with CFD. The solution procedure is iterative, and ensures strict time accuracy of response harmonics via trim iterations. It is therefore not the same as loose coupling as referred to in fixed-wing CFD/CSD. While the solution procedure is unique, the fluid-structure interface has been simple, so far, based on chord-wise integrated sectional airloads. A review of the state-of-the-art in rotorcraft CFD/CSD can be found in Ref.[15]

The coupling procedure in this paper is different from the state-of-the-art. An exact fluid-structure interface is implemented in this study – different from a conventional, sectional airloads based interface. An exact interface provides key advantages over the conventional. First, it is essential for advanced geometry blades, an example of which is the BERP blade, for which the method of sectional airloads is arbitrary. Second, the exact method is generic and applicable to both structured and unstructured fluid grids, including on-blade adaptive refinement. Third, the convention is not limited to beams, but is easily extendable to other structural models that include chordwise distortions or 3D geometry.

In the present interface, the blade is not excited by chord-wise integrated sectional airloads, the fluid stresses or the locally integrated stresses on each surface patch are imposed directly on the structure. This is accomplished easily by an exact calculation of virtual work. As such, the interface is conservative, and preserves the spatial order of accuracy of the worse solver. In addition, it preserves the total forces between the fluid and structural domains – a desirable, though not a necessary, condition. We call the interface preservative. Implementing the interface is straight forward, but the unique solution procedure in rotary-wing, based on the delta method,[16] that ensures strict time-accuracy of the response harmonics, now requires an innovative re-formulation. This is because there are no sectional *delta* airloads in an exact interface, and any attempt to create one, even by a consistent interpolation on an unstructured surface grid, destroys the exactness of the virtual work terms. In this paper, we provide a modification that implements the delta procedure exactly – via a simple change in the definition of delta quantities – without any requirement for a sectional calculation.

The paper is organized as follows. The theoretical background and the mathematical formulation of the time-spectral method are described in Section II-A. In Section II-B, we provide a detailed study of the accuracy, convergence and efficiency of the time-spectral method. Using uncoupled, CFD only calculations, with a prescribed set of blade deformations, we precisely quantify the aliasing errors. The exact CFD/CA coupling procedure is described in Section III along with a verification of the exact fluid-structure interface. The fully coupled CFD/CA results the presented in the last section followed by conclusions of the study.

II. TIME-SPECTRAL METHOD

A. Mathematical Formulation

The Navier-Stokes equations in a semi-discrete form can be written as

$$V\frac{\partial u}{\partial t} + R(u) = 0, \quad u = \begin{pmatrix} \rho \\ \rho u' \\ \rho v' \\ \rho w' \\ \rho E \end{pmatrix}, \tag{1}$$

where u is the vector of conservative variables, and $R(u)$ is the residual of spatial discretization of viscous, inviscid, and numerical dissipation fluxes. If we approximate u by a discrete Fourier series at N integer points,

$$u_j^N = \sum_{k=-N/2}^{N/2-1} \tilde{u}_k e^{ikt_j} \quad (j = 0, ..., N-1), \quad \text{where} \quad t_j = \frac{T}{N} j \ , \tag{2}$$

and T is a period, and u_j^N represents the truncated Fourier series of u up to N. A $\tilde{u}_k$ is a discrete Fourier coefficient of the variable u defined as follows,

$$\tilde{u}_k = \frac{1}{N}\sum_{j=0}^{N-1} u_j^N e^{-ikt_j} \quad k = -N/2, ..., N/2-1 \tag{3}$$

For the collocation method Equation 1 is required to be satisfied at each point,

$$\frac{\partial u_j^N}{\partial t} + R(u_j^N)|_{t=t_j}, \quad j = 0, 1, ..., N-1 \tag{4}$$

On the other hand, a differentiation of u in physical space can be obtained by the inverse transformation of the discrete Fourier coefficients multiplied by ik. Then the approximate derivative at the grid points are given by

$$(\mathcal{D}_N u)_l = \sum_{k=-N/2}^{N/2-1} a_k e^{ikt_l} \quad (l = 0, 1, ..., N-1), \quad \text{where } a_k = ik\tilde{u_k} = \frac{ik}{N}\sum_{j=0}^{N-1} u_j^N e^{-ikt_j} \tag{5}$$

Equation 5 can be reprented by a matrix form by combining two terms in Equation 5,

$$(\mathcal{D}_N u)_l = \sum_{j=0}^{N-1} (D_N)_{lj} u_j^N, \quad \text{where } (D_N)_{lj} = \frac{1}{N}\sum_{k=-N/2}^{N/2-1} ike^{ik(t_l - t_j)} \tag{6}$$

Application of Fourier collocation derivative type operator to Equation 4 renders it as below,

$$D_N U + R(U) = 0, \quad \text{where } U \text{ is a vector form of } (u_0^N,\ u_1^N, ..., u_{N-1}^N) \tag{7}$$

If a pseudo-time derivative term is directly added for a time integration, then Equation 6 can be represented as below,

$$V\frac{\partial u_j^N}{\partial \tau} + VD_N u_j^N + R(u_j^N) = 0 \ (j = 0, 1, 2, ..., N-1)\ . \tag{8}$$

and Equation 8 is the final form of the equation we are employing. Compared to the original Equation 1, Equation 8 has a simpler form as a steady-state formulation. A matrix form of derivative operator can be written as a closed form as below with a odd number of grid points (time instances),

$$(D_N)_{lj} = \begin{cases} \frac{1}{2}(-1)^{l+j} cosec(\frac{(l-j)\pi}{N}) & : l \neq 0 \\ 0 & : l = j\ . \end{cases} \tag{9}$$

This matrix is skew-symmetric and the corresponding eigenvalues are $ik,\ k = -(N-1)/2, .., (N-1)/2$, with a odd number N. If we have a odd number of time instances, then eigenvalue of zero has single multiplicity rather than double multiplicity in the case of even number of time instances. For this reason, we choose to have a odd number of time instances for spectral formulation in our study for a stability issue related to the eigenvalues.[7]

B. Convergence, Accuracy and Efficiency of Time-Spectral Method

The spectral accuracy is major attractiveness of the Fourier spectral method. Its convergence rate is ideally faster than any negative power of N, if u is N-times continuously differentiable and their derivatives up to $N-2$ are periodic. For example, the accuracy of the 2nd order finite-difference method with $N = 2048$ becomes equivalent to that of the spectral method with $N = 12$ for the ideal case. If the band-width of the underlying waveforms is known and the number of sampling points are more than double of the Nyquist frequency, then spectral accuracy can be achieved.

However, the real waveforms we encounter in rotor flow analysis, such as the sectional airloads, are highly nonlinear and not band-limited, smoothness of their variation in time is not guaranted, and the availability of the differentiation is not known a priori. Therefore the time-spectral method we apply for the rotor

flow analysis is inevitably under the influence of errors which are common to a classical Fourier collocation method, i.e. truncation error and aliasing error.

A precise quantification of those errors greatly depend on the smoothness of the original waveform we approximate and the periodicity of its derivatives. These errors are determined by the rate of decay of the Fourier coefficients in the frequency domain. Aliasing errors arise from approximating the solution by the discrete Fourier series rather than the continuous one, and the discrete Fourier mode at x_k is the same as at $(k + Nm)$ nodes for any integer m, where $k = -N/2, ..., N/2 - 1$ for the even number of N. It is known that if the function u is smooth, then the order of aliasing error is the same as the truncation error.[7] If the function is well approximated and smooth, then the effects of the aliasing errors becomes negligible.

Therefore the issues we would like to address before we apply the time-spectral method with enough confidence to the real rotor simulation problem is that: With respect to a varying number of time instances, 1) how is the convergence of the solutions? 2) how accurate are the solutions? 3) how much of computational time savings can we have to preserve a certain level of accuracy?

In response to these questions, we conducted straightforward numerical experiment to see the effects of those errors on time-spectral simulation of rotor flows. Using well-resolved sectional airloads predicted by the conventional time-accurate method and their corresponding discrete Fourier coefficients obtained by DFFT (Discrete Fast Fourier Transform) of the original solutions, we attempted to reconstruct the aliased solutions by including only a certain number of Fourier coefficients. The reconstructed aliased time-accurate solutions are, then, compared with the time-spectral solutions with different number of time instances.

A Counter 8534 of the steady level flight of UH-60A configuration is simulated by both time-accurate and time-spectral methods. A full wake capturing approach using an isolated rotor with 4 blades is employed. For this parameter study, we use rather coarse grid with 2.4 million nodes, but all other computations later are performed using a finer grid with about 17 million nodes. A conventional 2nd order BDF scheme with a time step of 0.5 has been used to resolve the periodic solutions of rotor flows, although Figure 1 shows time-accurate solutions at every 4^o. A different number of time instances varying from 3, 5, 9, 11, 15, to 25 is used for time-spectral simulation. Figure 1, and 2 show the sectional pitching moment at 96.5 % radial location. Figure 1 shows the time-spectral and time-accurate solutions, and their spectrally interpolated solutions for the time-spectral computation are shown at Figure 2.

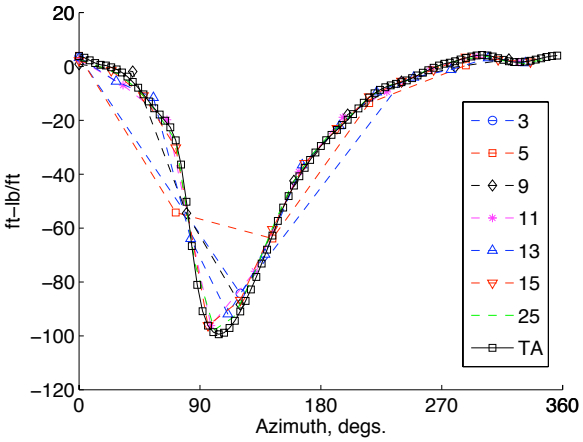

Figure 1. Time-Spectral solution of predicted pitching moment at 96.5% R using prescribed deformations; high speed flight C8534 of UH-60A

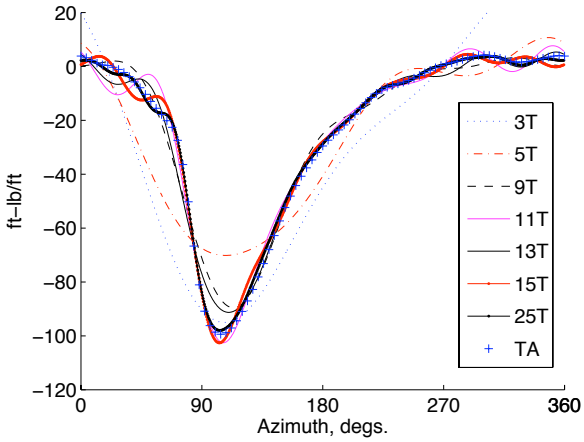

Figure 2. Spectral reconstruction of predicted pitching moment at 96.5% R using prescribed deformations; high speed flight C8534 of UH-60A

Waveform of the airloads we assume to be accurate or exact for comparison purpose is obtained from the finite-difference computation with the time-step of 0.5 i.e., a total of 720 sample points. However, observing that the higher harmonics of the frequency content are negligible, we include the harmonics only up to 44/rev just for a simplicity of the numerical test. With this value of Nyquist frequency the exact reconstruction of the original waveform requires a total of 88 sample points, i.e. two per wavelength, based on Nyquist Shanon sampling theorem, and any waveform reconstructed with less number of sample points contain aliasing errors.

The quantification of the aliasing error is possible by considering an infinite number of mirror images

centered at the integer multiple of the sampling rate. Figure 3 shows the the spectra of the original function with Nyquist frequency of 44/rev and the mirror images corresponding to the the sampling rate of 11 that is less than Nyquist sampling rate of 88. Instead of including an infinite number of mirror images ranging $(-\infty \sim \infty)$, the most influential two mirror images are constructed to approximately quantify the aliasing errors, which come from the frequencies in the images folding back into the spectrum of the original waveform.

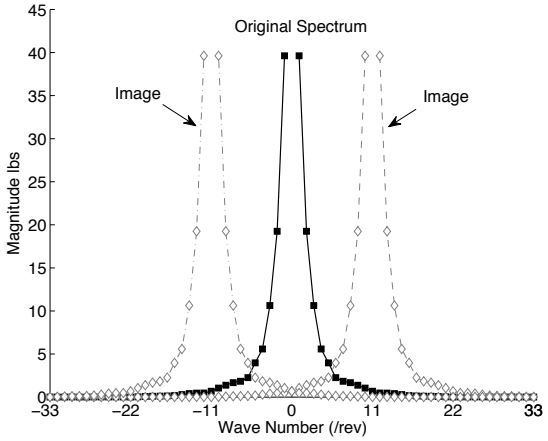

Figure 3. An example spectra plot of the Fourier coefficients of the original function and its mirror images (pitching moments at 96.5% radial location with sampling rate of 11 below than the Nyquist rate of 88.)

In a similar way, a series of spectrum plots with mirror images are constructed corresponding to a different number of sampling rates. To estimate the aliasing errors between the original waveform (which is assumed to be exact with 88 sampling rate) and the reconstructed waveform with the sampling rate less than Nyquist rate, we calculated L^2 norm of the differences in magnitudes of the discrete Fourier coefficients between the exact waveform and the aliased waveform. It is divided by the L^2 norm of all Fourier coefficients of the exact waveform so that it can represents the percentile error. This error criterion is basically equivalent to measuring pointwise errors in the physical domain. These percentile L^2 norms are plotted as the solid lines at Figure 4.

For the time-spectral solutions, we simply computed the percentile L^2 norm of the differences in the magnitudes of discrete Fourier coefficients of the time-spectral solutions and the exact time-accurate solutions. These L^2 norm values are plotted as the symbols of square in Figure 4. Each symbol corresponds to the different number of time instances varying from 3, 5, 9, 11, 13, 15 to 25. This analysis has been performed for sectional pitching moment waveforms at raidal locations at 10, 55, 86.5 and 96.5 % and the comparison of L^2 norms between time-accurate and time-spectral solutions are shown at Figure 4.

We can infer from Figure 4 several significant facts related to the convergence and accuracy of the time-specral method. First, the errors from time-spectral solutions with a varying number of time instances are very close to the predicted errors by the aliased time-accurate solutions. In theory, the errors from time-spectral and aliased time-accurate should be the same, however the amount of discrepancy is little. This can be explained by the fact that we include only two most adjacent mirror images to quantify the aliasing errors. The level of solution convergence in time-accurate and time-spectral solution may not exactly coincide. Second, we can infer from the error behaviors of the aliased time-accurate solutions the characteristics of the time-spectral solution on the accuracy and the convergence with respect to the number of time instances. As the number of time instance increases, the norm of the errors between aliased and non-aliased time-accurate solutions approaches to zero at a rate similar to the spectral convergence rate or exponential rate.

The key conclusions we can make on the convergence and accuracy of the time-spectral method are that: 1) the aliasing error decreases as we increase the number of time instances. 2) convergence rate is nearly exponential as the number of time instances increases. 3) With the number of time instances as small as around 20, we can achieve the accuracy within $1 \sim 2\%$ errors. Also this number of time instances can resolve the phenomena dominated by the critical vibratory frequencies (3,4,5 /rev and 7,8,9 /rev).

However, it should be noted that this conclusion can not be generalized for all cases of rotor flow analysis. The convergence and accuracy of the time-spectral method greatly depend on the characteristics of the

airloads waveform. Therefore if the airloads do not show smooth variation during a period, then the effects of the aliasing errors may not be negligible even with reasonably large number of time instances.

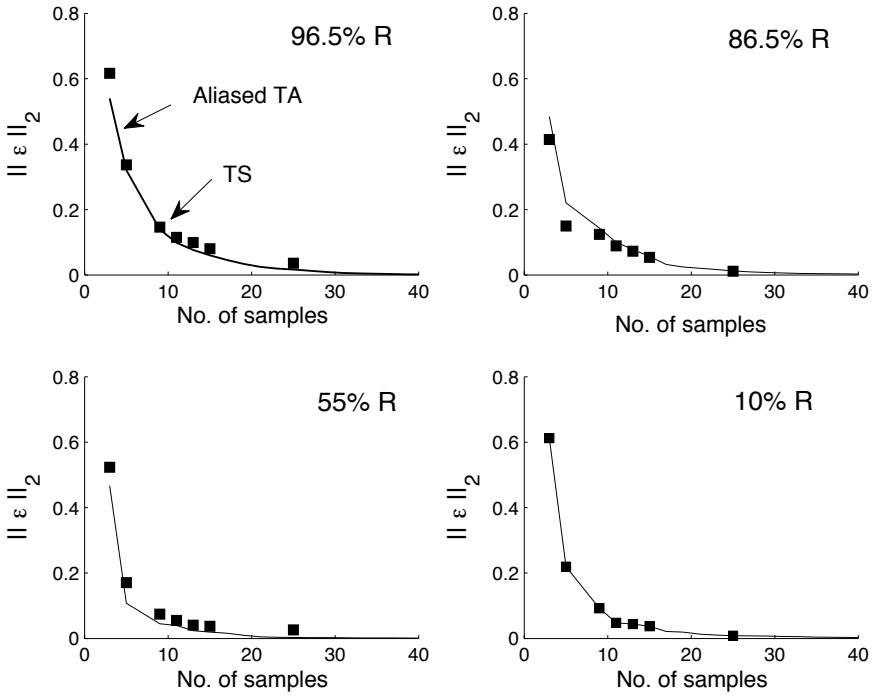

Figure 4. L^2 **norm of the differences in magnitude of Fourier coefficients among aliased time-accurate, non-aliased time-accurate, and time-spectral solutions.**

The final question to be addressed is the efficiency of the time-spectral method that is closely related to the accuracy of the method. Compared to the finite-difference method which typically requires around hundreds or thousands of time steps per period, the time-spectral method needs a number of time instances less than about twenty with the accuracy almost equivalent to that of the finite-difference method (see Figure 4).

However, if higher accuracy with more number of time instances is desired, the increase in time and memory is unavoidable. A wall-clock CPU time per multigrid cycle (3w in our case) with respect to a different number of time instances is plotted at Figure 5. As the number of time instance increases, the time increment is not linear and its slope is gradually increasing. A computation time for a multigrid cycle is the addition of time for space discretization and for spectral derivative term (see Equation 8), and is typically dominated by the space discretization which have operating counter of $O(N)$ for the finite-difference method. Thus, at a small number of time instances, computation time for the spectral derivative term is negligible and increase in time is dominated mostly by linear contribution from space discretization. However, as the number of time instances becomes large, computation time for the derivative term with operating counter of $O(N^2)$ (of multiplication of matrix and vector) can not be neglected and the quadratic increase is gradually reflected in total time.

A direct comparison of total wall-clock CPU time is made between time-accurate and time-spectral computation to see the efficiency of the time-spectral method. A total wall-clock CPU time to obtain the converged solutions is estimated for both computation methods. For time-accurate method using the 2nd order BDF scheme, a time step of about $0.25 \sim 0.5^o$, pseudo time integration of about $20 \sim 30$ multigrid cycles, and time marching up to $1.5 \sim 2$ revolutions are required for the entire simulation. Time-spectral method has shown to converge after $700 \sim 1,200$ multigrid cycls for pseudo time integration.[4] A total of 128 processors of IBM P4+ computer clusters are used. Time-spectral computation with a total of 11 time instances takes about 15.65 seconds to complete one multigrid cycle and time-accurate computation takes about 1.47 seconds per multigrid cycle. Thus the total estimated computation time for

time-spectral simulation ranges in 15.65 sec $\times$ (700 $\sim$ 1500 iterations) $= 10,955 \sim 23,475$ seconds. Time-accurate simulation can be estimated as $(1.5 \sim 2)\text{rev} \times 360^o/(0.25 \sim 0.5^o)\text{deg} \times (20 \sim 30)\text{iterations} \times 1.47\text{sec} = (31,752 \sim 127,008)$ seconds. Time saving factor between time-accurate and time-spectral computation for this particular example varies between 2.9$\sim$ 5.1.

The details of the computation procedure depends on the types of the problem we attempt to solve, i.e. whether it requires a small number of time step size over a few number of revolutions, etc. A rigorous comparison between the two methods, thus, requires a certain degree of flexibility considering the characteristics of the problems we solve and the level of convergence we want to achieve. Nevertheless time-spectral computation has shown more than the factor of at lease two or three for all simulations in our previous[4,6] and the current simulation using up to as many as 25 time instances.

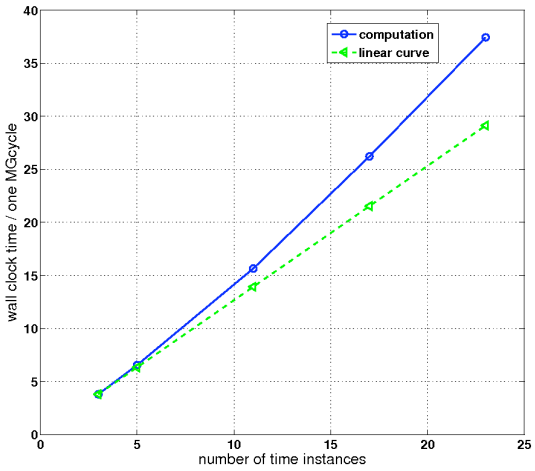

Figure 5. Wall clock time per one multigrid cycle w.r.t. the number of time instances varying from 3, 5, 13, 17 to 23.

C. Implementation: SUmb solver

Three-dimensional compressible Navier-Stokes flow solver, SUmb (Stanford University multi-block), has been utilized for all computations in this paper. SUmb is a multi-block structured flow solver developed at Stanford University under the sponsorship of the Department of Energy Advanced Strategic Computing (ASC) program. Various turbulence models are implemented to capture the viscous and turbulent properties of the flow: Baldwin-Lomax, Spalart-Allmaras, $k-\omega$, Menter SST, v^2-f. SUmb is a massively parallel code (in both CPU and memory) using scalable pre-processor, load balancing, and MPI. It employs multigrid, Runge-Kutta time stepping for the mean flow, and DD-ADI solution methodology for the turbulence equations. Central difference discretization (second order in space) with several artificial dissipation options (scalar or matrix), or upwind discretization is available for a space discretization. For unsteady time integration, second-/third-order backwards difference formula(BDF) or the time-spectral approach for time-periodic flows can be used. SUmb has been successfully used in many applications including simulation of launch vehicles, space and re-entry vehicles, jet/turbo engines, subsonic and supersonic aircraft, and helicopters. A second order BDF scheme was used for the time-accurate computation, and a second order upwind scheme with Roe's flux differencing for the inviscid fluxes. Spalart-Allmaras turbulence model was used for the computation of the viscous flux and the turbulence.

III. CFD/Comprehensive Analysis Coupling

This section describes the two key components of exact coupling. First, the formulation of an exact interface is described, followed by a simple verification. Then, a modified delta coupling procedure is formulated to accompany the exact interface. Validation of the exact coupling procedure using coupled CFD/CA analysis is shown later in the section on Results.

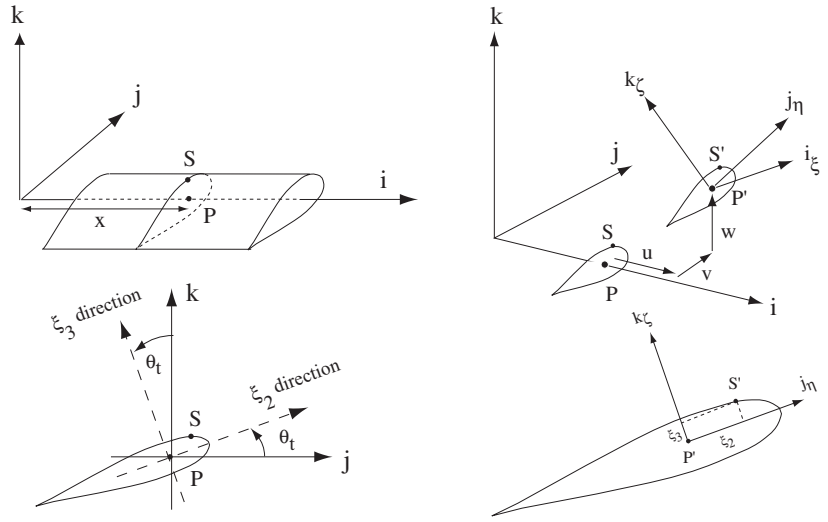

(a) Blade section before deformation

(b) Blade section after deformation

Figure 6. Blade cross-section and surface geometry before and after deformation

We note that the exact procedure includes two other requirements: exact deformation transfer to CFD, in space and time; and exact airload transfer from CFD, in time. Both are easily implemented using the spatial and temporal shape functions of the present CSD model, and is not part of the present discussion.

A. Exact Fluid-Structure Interface

An exact interface begins with a surface geometry representation followed by an exact virtual work calculation. In the case of a single component structure, like a rotor blade, the surface geometry is easily represented using the underlying structural model.

Consider the undeformed blade surface geometry in Fig. 6(a). The surface point S is located at a cross-section P on the undeformed beam elastic axis. Assume that the principle axes of the section lie along ξ_2 and ξ_3 directions, at an angle θ_t with respect to an undeformed coordinate system. θ_t is the built-in structural twist. If the undeformed coordinate system is defined by the unit orthogonal base vectors $\mathbf{e}^0 = [ijk]^T$, then the surface coordinates are given as

$$\vec{r}_S = \left\{ \begin{array}{c} x \\ \xi_2 \cos\theta_t - \xi_3 \sin\theta_t \\ \xi_2 \sin\theta_t + \xi_3 \cos\theta_t \end{array} \right\}^T \left\{ \begin{array}{c} i \\ j \\ k \end{array} \right\} \tag{10}$$

where $S = S(x, \xi_2, \xi_3)$ provides an unique surface parameterization. The section after deformation is shown in Fig. 6(b), where S has now moved to S'. Let the deformed coordinate system is defined by the base vectors $\mathbf{e}^d = [i_\xi, j_\eta, k_\zeta]^T$. The vectors j_η and k_ζ are chosen along the principal axes of the deformed section (as the structural properties are known about them), and the third is defined by

$$i_\xi = j_\eta \times k_\zeta$$

The section undergoes translation and rotation but the position of S' is defined uniquely by these deformations and the surface parameters $S(x, \xi_2, \xi_3)$. In the case of no cross-sectional distorsions, the surface point S' maintains the same relative position with respect to the principal axes, as illustrated in Fig. 6(b). However, the convention here is extendable to generic models using chordwise distortions or 3D geometry. The deformed position of the surface point S' is given by

$$\vec{r}_{S'} = \left\{ \begin{array}{c} x + u_1 \\ u_2 \\ u_3 \end{array} \right\}^T \left\{ \begin{array}{c} i \\ j \\ k \end{array} \right\} + \left\{ \begin{array}{c} \lambda\Psi \\ \xi_2 \\ \xi_3 \end{array} \right\}^T \left\{ \begin{array}{c} i_\xi \\ j_\eta \\ k_\zeta \end{array} \right\} \tag{11}$$

where $\lambda(x)$ is a warp amplitude and $\Psi(\xi_2, \xi_3)$ a warp function. The deformed coordinates are related to the undeformed coordinates via a direction cosine matrix $\mathbf{C}$.

The direction cosine matrix $\mathbf{C}$ is intrinsic to the structure, determined only by the loading and boundary conditions. Its parameterisation takes various forms depending on the choice of parameters. In terms of a general C matrix, the position vector of S' becomes

$$\vec{r}_{S'} = \left\{ \begin{array}{c} x + u_1 + \lambda\Psi C_{11} + \xi_2 C_{21} + \xi_3 C_{31} \\ u_2 + \lambda\Psi C_{12} + \xi_2 C_{22} + \xi_3 C_{32} \\ u_3 + \lambda\Psi C_{13} + \xi_2 C_{23} + \xi_3 C_{33} \end{array} \right\}^T \left\{ \begin{array}{c} i \\ j \\ k \end{array} \right\} \tag{12}$$

The virtual displacement $\delta\vec{r}_{S'}$ can be obtained from equation 12 by taking variations with respect to the states. Let the states be three displacements u_1, u_2, u_3, and three rotation parameters $\theta_1, \theta_2, \theta_3$ – in the rotating frame. Note that for a case with shaft dynamics the virtual displacements are to be taken in a frame which includes the additional states of shaft dynamics, for example a fuselage fixed frame. Taking variations of each of the C_{ij} components as

$$\delta C_{ij} = \frac{\partial C_{ij}}{\partial \theta_1}\delta\theta_1 + \frac{\partial C_{ij}}{\partial \theta_2}\delta\theta_2 + \frac{\partial C_{ij}}{\partial \theta_3}\delta\theta_3$$

we have the virtual displacement in the following form

$$\delta\vec{r}_{S'} = (\mathbf{D}\delta\mathbf{u})^T \mathbf{e}^0 \tag{13}$$

where $\delta\mathbf{u}$ are the variations in six states

$$\delta\mathbf{u} = [\delta u_1, \delta u_2, \delta u_3, \delta\theta_1, \delta\theta_2, \delta\theta_3]^T$$

and D is a matrix of derivatives of size (3×6). The exact calculation of virtual work can now be carried out using fluid stresses at the surface. Consider a differential area $d\vec{A}$ within the surface patch $\Delta\vec{A}$ of magnitude

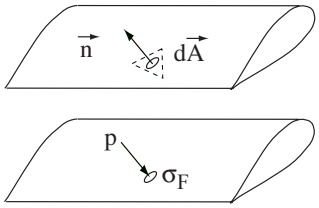

Figure 7. Fluid pressure and surface shear over a rotor blade differential area $d\vec{A}$

dA and unit normal $\vec{n}$, Fig. 7.

$$d\vec{A} = \vec{n}dA = \mathbf{n}^T\mathbf{e}^0 dA \tag{14}$$

The differential force generated by the pressure is

$$-pd\vec{A} = -p\mathbf{n}^T\mathbf{e}^0 dA$$

The differential force generated by the fluid stress tensor along the direction of $d\vec{A}$ is

$$\sigma_\mathbf{F} \cdot d\vec{A} = \sigma_\mathbf{F} \cdot \vec{n}dA = (\sigma_\mathbf{F}\mathbf{n})^T\mathbf{e}^0 dA$$

The virtual work is then

$$\begin{aligned} \delta W &= \int_{\Delta A} \left(-p\, d\vec{A} + \sigma_\mathbf{F} \cdot d\vec{A}\right) \cdot \delta\vec{r}_P \\ &= \int_{\Delta A} \left[-p\,\mathbf{n}^T + (\sigma_\mathbf{F}\mathbf{n})^T\right] \mathbf{e}^0 \cdot (\mathbf{D}\delta\mathbf{u})^T \mathbf{e}^0 dA \end{aligned} \tag{15}$$

If q are the N generalized nodal displacements of a finite element containing the point P, and $\mathbf{H}$ is the $(6 \times N)$ elemental shape function matrix, it follows from $\delta u = \mathbf{H}\delta q$

$$\delta W = \int_{\Delta A} \left[-p\,\mathbf{n}^T + (\sigma_F\mathbf{n})^T\right] \mathbf{D}\mathbf{H}\delta\mathbf{q}dA = \mathbf{Q}^T\delta\mathbf{q} \tag{16}$$

where the generalized force $\mathbf{Q}$ is

$$\mathbf{Q} = \int_{\Delta A} \left[-\mathbf{H}^T \mathbf{D}^T \mathbf{n}\, p + \mathbf{H}^T \mathbf{D}^T \sigma_F\, \mathbf{n} \right] dA \tag{17}$$

The integration involves variables from both domains. If performed in the fluid domain, exact values of $\mathbf{D}$ and $\mathbf{H}$ must be transferred from the structural domain to the fluid node (or face) points. If performed in the structural domain, exact values of p and σ_F must be transferred from the fluid domain at the structural Gauss points. The value of $\mathbf{n}$ will be different in both domains (except in the ideal case when the meshes and spatial orders match exactly). There have been significant contributions by various researchers to address the issue of conservation and preservation, within the context of temporal accuracy. See for example, Maman and Farhat,[21] Cebral and Lohner,[22] Farhat et al.,[23] Slone et al,[24] and Michler et al.[25] The key conclusion is that exact conservation is ensured only when interpolations of all the variables are performed using schemes consistent with their domain. Preservation of total forces occurs only in the limit of mesh refinement.

A counterpart of this method is one which preserves the total forces exactly – regardless of mesh size, but the work calculation is now exact only in the limit of mesh refinement. However, consistent interpolation is easier (with less transfer across domains) to ensure in this method. This is the case for a force interface where the fluid stresses are first integrated over each surface patch (in fluid domain) and then used to calculate virtual work (in structural domain). We call this the patch force interface. The following integration is performed in the fluid domain

$$\begin{aligned} \vec{F} &= \int_{\Delta A} -p\, d\vec{A} + \sigma_{\mathbf{F}} \cdot d\vec{A} \\ &= \left[-\int_{\Delta A} p\, \mathbf{n}^T\, dA + \int_{\Delta A} (\sigma_{\mathbf{F}} \mathbf{n})^T\, dA \right] \mathbf{e}^0 = \mathbf{F}^T \mathbf{e}^0 \end{aligned} \tag{18}$$

where the force $\mathbf{F} = [F_1, F_2, F_3]^T$ has been expressed in the same basis. Obviously, the total forces remain the same when transferred from the fluid to the structural domain. However, because the point of application of $\vec{F}$ within each surface patch is arbitrary, the method is conservative only in the limit of mesh refinement. The virtual work by a surface force $\vec{F}$ acting at S' is simply

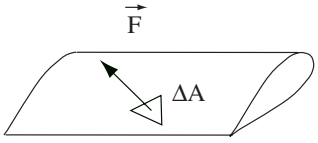

Figure 8. A patch force on a rotor blade obtained by integrating fluid pressure and surface shear over an area ΔA

$$\delta W = \vec{F} \cdot \delta \vec{r}_{S'} \tag{19}$$

where $\delta \vec{r}_{S'}$ is a virtual displacement of the point S'. In terms of states and generalized coordinates

$$\delta W = \mathbf{F}^T \mathbf{D} \delta \mathbf{u} = \mathbf{F}^T \mathbf{D} \mathbf{H} \delta q = \mathbf{Q}^T \delta \mathbf{q} \tag{20}$$

where the generalized force is

$$\mathbf{Q} = \mathbf{H}^T \mathbf{D}^T \mathbf{F} \tag{21}$$

The term $\mathbf{D}^T$ transmits the airloads in 3-D space to the 1-D beam structure. The matrix D varies with the choice of beam theory. Note that, from eqn. 13, the virtual displacement components are

$$\delta \mathbf{r}'_S = \mathbf{D} \delta \mathbf{u} = \mathbf{D} \mathbf{H} \delta \mathbf{q} \tag{22}$$

Equations 21 and 22 highlight the well-known relation that the generalized structural forcing vector relate to the aerodynamic forcing via the transpose of the relation that connects the aerodynamic deflections to structural deflections. Here, $\mathbf{DH}$ can be interpreted as the equivalent elemental shape functions in 3-D space for the corresponding beam theory.

B. Verification of Interface

The objective here is to start from the exact interface and illustrate the necessary simplifications so as to re-produce the sectional airloads from surface pressures via the interface. This procedure is possible as the CFD grid is structured.

The structural model is a second-order nonlinear Euler-Bernoulli beam based on the classical formulations of Refs.[26–28] Only one orientation angle remains an independant state, the rest are expressed as functions of the displacement gradients. Warping is ignored. Denoting the displacements as $u_1 = u$ (axial), $u_2 = v$ (lead-lag), and $u_3 = w$ (flap); and retaining up-to second order non-linearities; the direction cosine matrix takes the following standard form

$$C = \begin{bmatrix} 1 - \frac{v'^2}{2} - \frac{w'^2}{2} & v' & w' \\ -v'c - w's & (1 - \frac{v'^2}{2})c - v'w's & (1 - \frac{w'^2}{2})s \\ v's - w'c & -(1 - \frac{v'^2}{2})s - v'w'c & (1 - \frac{w'^2}{2})c \end{bmatrix} \tag{23}$$

where $c = \cos\theta; s = \sin\theta$, and $()'$ is derivative along undeformed elastic axis. The orientation angle θ can be expressed in two parts – a rigid contribution from built-in twist and control angles θ_t, and an elastic twist deformation $\hat{\phi}$ that is a quasi-coordinate.

$$\theta = \theta_t + \hat{\phi}$$

$$\hat{\phi} = \phi - \int_0^x w'v''dx + O(\epsilon^3)$$

where the angle ϕ is defined such that the torsion, κ_i, i.e. the total angle of twist per unit length of the deformed elastic axis, is given by

$$(\theta_t + \phi)^+ = \kappa_i; \qquad \theta_t^+ = \theta_t' x^+$$

Here $()^+$ is the derivative along the deformed elastic axis. Note that the torsion moment is given by $GJ\phi'$ or $GJ(\hat{\phi}' + w'v'')$.

The virtual work is now expressed in terms of the following variations.

$$\delta W = F_u\delta u + F_v\delta v + F_w\delta w + M_{w'}\delta w' + M_{v'}\delta v' + M_{\hat{\phi}}\delta\hat{\phi} \tag{24}$$

where

$$F_u = F_1; \qquad F_v = F_2; \qquad F_w = F_3 \tag{25}$$

and

$$\begin{aligned} M_{w'} =& (-\xi_2 c - \xi_3 c)\, F_1 + \\ & (-v'\xi_2 s - v'\xi_3 c)\, F_2 + \\ & (-w'\xi_2 s - w'\xi_3 c)\, F_3 \\ \\ M_{v'} =& (-\xi_2 c + \xi_3 s)\, F_1 + \\ & [-\xi_2(-v'c - w's) + \xi_3(v's - w'c)]\, F_2 \\ \\ M_{\hat{\phi}} =& [\xi_2(v's - w'c) + \xi_3(v'c + w's)]\, F_1 + \\ & \left[\xi_2\left\{(1 - v'^2/2)s - v'w'c\right\} + \xi_3\left\{-(1 - v'^2/2)c + v'w's\right\}\right] F_2 + \\ & \left[\xi_2(1 - w'^2/2)c - \xi_3(1 - w'^2/2)s\right] F_3 \end{aligned} \tag{26}$$

These are the exact beam forcing corresponding to a patch force $\vec{F}$ at a surface point S' on the *deformed* blade, where S' corresponds to the surface point $S = S(x, \xi_2, \xi_3)$ on the *undeformed* blade. F_u provides forcing for the state u, F_w for w, and F_v for v. The radial moment terms $M_{w'}$ and $M_{v'}$ are to be used only when shear states are included. These are small terms , 5% to 10% of $M_{\hat{\phi}}$. $M_{\hat{\phi}}$ is the dominant term, the forcing for elastic twist. Its largest contributing component is

$$M_{\hat{\phi}} \approx -(\xi_2 s + \xi_3 c)F_2 + (\xi_2 c - \xi_3 s)F_3 \tag{27}$$

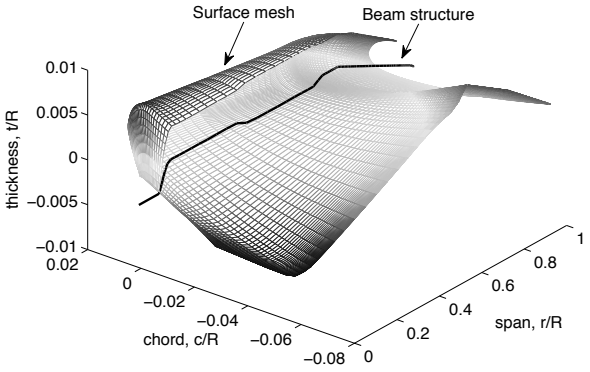

Figure 9. The CFD surface grid cut-out showing the embedded CSD beam model

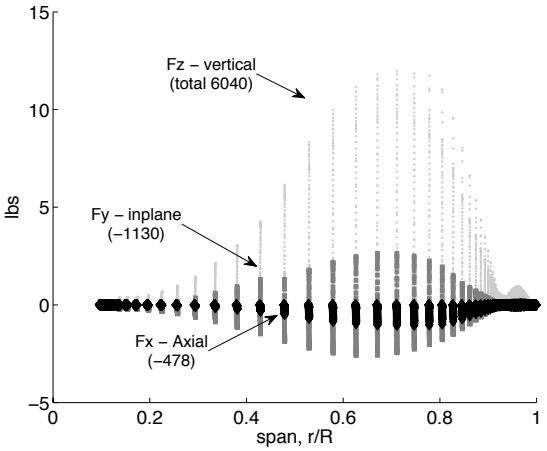

Figure 10. Patch forces on the blade at $\psi = 0^o$ azimuth; taken from C8534 UMARC-SUmb TA coupled solution

that is readily recognised as the pitching moment contribution of $\vec{F}$ about the elastic axis at x. Note that the coordinate x is uniquely determined by the parameterization of the surface point. It is built on the underlying structural model, and thus there is no ambiguity for an advanced geometry blade.

Figure 9 shows the CSD beam within the CFD surface mesh in the present study. The patch coordinates are taken at the centers of the surface nodes. The surface is parameterized as $S(x, \xi_2, \xi_3)$ using Eq. 10. A converged UMARC-SUmb solution (shown later in Results section) is used is for verification. The flow solution is used to extract the surface patch forces $\vec{F}$ (see Fig. 10). The blade deformations are then be used to calculate the exact forcing terms following Eqs. 25 and 26.

For verification purposes, an arbitrary set of radial points x_p (see Fig. 11) are taken on the beam. The directly integrated sectional airloads are then compared at these stations with those *reduced* from the exact interface. During this reduction, $M_{\hat{\phi}}$ is calculated from the approximate expression in Eq. 27. The F_u, F_v, F_w, and $M_{\hat{\phi}}$, calculated at every x, are then distributed between its two neighboring x_p points linearly based on distance. The sectionally integrated airloads at those points are then compared with the reduced beam forces divided by Δx_p. If the CFD grid is structured, the points x_p coincident with the spanwise grid sections, and if the expression given in Eq. 27 is used, then both must be identical. For a limited set of x_p, a set of 27 points as used here for illustration, they are expected to differ because the reduced beam forces contain each and every patch force contribution, whereas the sectional airloads include only the sectional distribution. An example is shown in Fig. 12. The quarter-chord pitching moment at a section on the swept tip is compared between the two methods.

C. Modified Delta Procedure

The modified delta procedure is formulated in the same manner as the original, but the *delta*'s are now taken between two finite element quantities. Two *delta* quantities are required - one used during response calculation, and another during hub loads calculation.

The need for two *delta* quantities is evident from the of the original construction of the method. The method requires that a lower order aerodynamic model be retained which can provide airload sensitivities to blade deformation. The purpose is to shift the burden of trim to this lower order model while replacing it iteratively with CFD. The resulting procedure is very efficient for rotorcraft because the airload sensitivities also supply the necessary damping for a direct extraction of response harmonics – a reliable and efficient means for calculating periodic response of a system that lies at or close to resonance with very little structural damping. The two *delta* quantities in the present method are constructed to preserve these two ideas.

The first *delta* is constructed during the response calculation. It is the difference between two finite element generalized forcing $\mathbf{Q}$ (see Eq. 21) – one from CFD patch forces and another from lifting-line

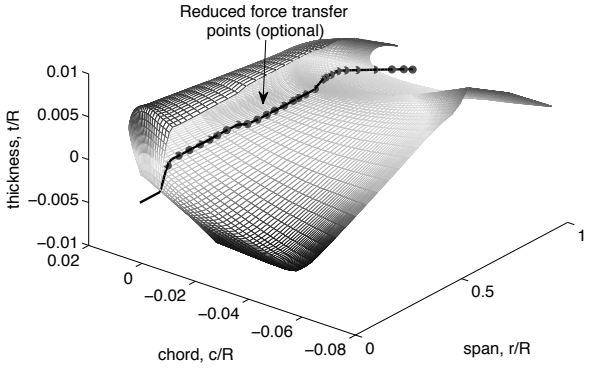

Figure 11. CFD surface grid, CSD beam model, and generic force points for a reduced interface

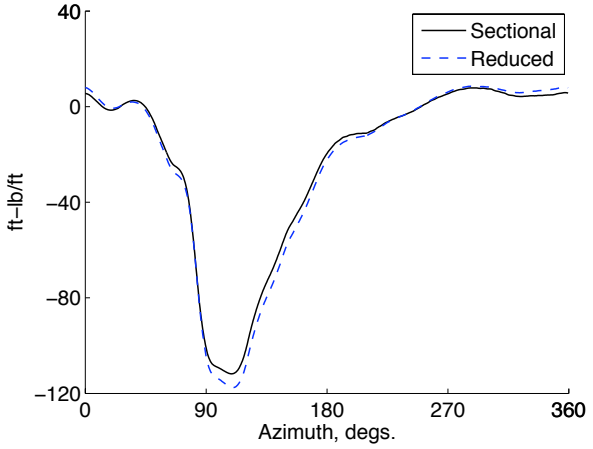

Figure 12. Verification of exact interface; 1/4-c pitching moment at 96.5%R; Sectional integration vs. reduction from exact forcing

sectional airloads.

$$^{q}\mathbf{\Delta} = \mathbf{Q}^{CFD} - \mathbf{Q}^{LL}$$

Each quantity arises out of an exact integration in its own domain. There is no requirement to interpolate one on the other. The second *delta* is constructed during hub loads calculation for trim angle update. It is the difference between two finite element integrated loads – one from CFD and another from lifting-line airloads.

$$^{h}\mathbf{\Delta} = \mathbf{h}^{CFD} - \mathbf{h}^{LL}$$

Again, the integration is exact, seperately, within the CFD and lifting-line domains with no requirement to interpolate one on the other. The coupling method then follows exactly the same original steps.

1. Perform baseline lifting-line (LL) analysis. Store $\mathbf{Q}_0 = \mathbf{Q}_0^{LL}$, and elemental integrated loads $\mathbf{h}_0 = \mathbf{h}_0^{LL}$.

2. Use deformations to calculate CFD solution.

3. Impose CFD patch forces on CSD. Do not calculate response. Instead, Calculate $\mathbf{Q}_0^{CFD}$, $\mathbf{h}_0^{CFD}$.
   Obtain $^{q}\mathbf{\Delta}_0 = \mathbf{Q}_0^{CFD} - \mathbf{Q}_0^{LL}$; $^{h}\mathbf{\Delta}_0 = \mathbf{h}_0^{CFD} - \mathbf{h}_0^{LL}$.
   Re-perform lifting-line analysis with $^{q}\Delta_0$ added to intrinsic forcing during response, and $^{h}\mathbf{\Delta}_0$ added to elemental loads during hub loads calculation. Total forcing is $\mathbf{Q}_1 = \mathbf{Q}_1^{LL} + \mathbf{\Delta}_0$ where $\mathbf{Q}_1^{LL}$ contains aerodynamic damping. Total hub loads is $\mathbf{h}_1 = \mathbf{h}_1^{LL} + \mathbf{\Delta}_0$ where $\mathbf{h}_1^{LL}$ contains trim sensitivities.

Steps 2 and 3 form one coupling iteration. These are repeated for $k = 1, 2, \ldots$. For example, in each iteration, the delta and total generalized forcing are given by

$$\begin{aligned} ^{q}\mathbf{\Delta}_k &= \mathbf{Q}_k^{CFD} - \mathbf{Q}_k^{LL}; \qquad \mathbf{Q}_{k+1} = \mathbf{Q}_{k+1}^{LL} + {}^{q}\mathbf{\Delta_k} \\ ^{h}\mathbf{\Delta_k} &= \mathbf{h}_k^{CFD} - \mathbf{h}_k^{LL}; \qquad \mathbf{h}_{k+1} = \mathbf{h}_{k+1}^{LL} + {}^{h}\mathbf{\Delta}_k \end{aligned} \tag{28}$$

Alternatively, the delta quantities can be updated as

$$^{q}\mathbf{\Delta}_k = \mathbf{Q}_k^{CFD} - (\mathbf{Q}_k - {}^{q}\mathbf{\Delta}_{k-1}) = {}^{q}\mathbf{\Delta}_{k-1} + (\mathbf{Q}_k^{CFD} - \mathbf{Q}_k) \tag{29}$$

Both are identical, only the stored variable is different, one may be preferred over the other for a particular analysis. The first requires the total and delta quantities be stored in every iteration. The second requires the lifting-line contributions be seperated out and stored in every iteration. In this study, the second storage was easier.

The procedure terminates when the *delta*'s converge (both necessarily converge at the same time). On convergence both the response as well as trim are satisfied entirely by the CFD airloads.

D. Implementation: UMARC Comprehensive Analysis

The exact coupling is implemented using the University of Maryland Advanced Rotorcraft Code — UMARC.[17] It provides the CSD and trim capabilities, and in addition, the aerodynamic sensitivities to blade deformations as required by the coupling procedure. The details of the model, methodologies, and validation can be found in Ref.[18] The UH-60A rotor model, and the analysis is identical to the one used for the original CFD/Comprehensive Analysis coupling studies with the UMTURNS code.[19,20] The periodic CSD response is extracted using finite elements in time. Twelve finite elements are used over one revolution, each containing six nodes with fifth-order mixed Lagrange-Hermite interpolating shape functions.

The trim procedure used is an isolated rotor targetted trim, not a full aircraft trim as in the above references. The three rotor control angles are determined from a target thrust and the two hub moments, pitch and roll, at a prescribed set of shaft tilt. The targetted thrust, hub moments, and the shaft angles are estimated or measured from flight test (see Results section).

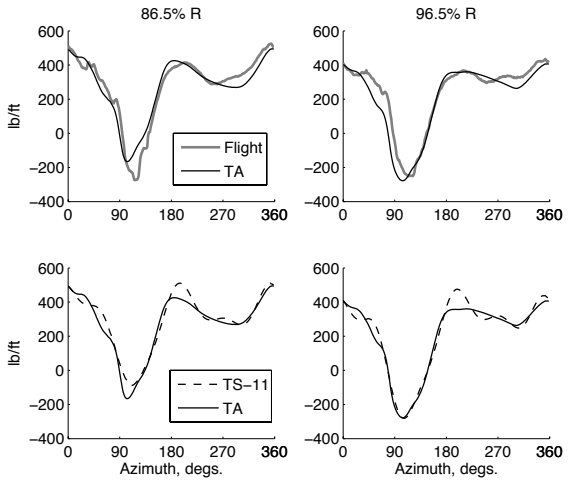

Figure 13. Measured and predicted normal forces for the UH-60A in high speed flight C8534

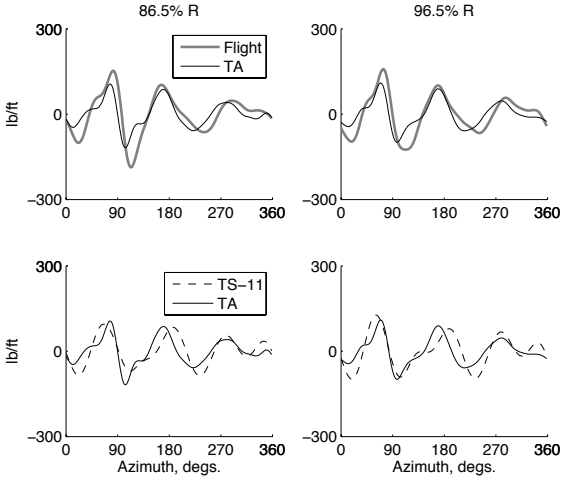

Figure 14. Measured and predicted vibratory normal forces (3-20 /rev) for the UH-60A in high speed flight C8534

IV. RESULTS

The high-speed flight Counter 8534 from the U. S. Army/NASA UH-60A Airloads Program is chosen for validation: speed ratio $\mu = 0.368$ (155 kts), vehicle weight coefficient to solidity ratio $C_W/\sigma = 0.0783$, and a longitudinal shaft tilt angle of $\alpha = 7.31°$ (tilt-forward). The predicted thrust level (along shaft) for this flight is $C_T/\sigma = 0.084$, around 17,500 lb. The measured rotor roll and pitch moments (from shaft bending gages) are around 6000 ft-lb (roll left) and 4200 ft-lb (pitch up) respectively.

There are several reasons for choosing this flight. It is one of the highest vibration flights for this helicopter, with high levels of rotor vibratory loads. The contribution of CFD is most significant in this flight. The fundamental mechanisms of vibratory loads in this flight are, also, well documented.[18] The primary mechanism of vibratory airloads in this flight is the large elastic twist deformation of the blade in response to three-dimensional, unsteady, transonic pitching moments near the tip on the advancing side. The secondary mechanism, occurring in presence of the correct twist, is an inboard wake interaction on the advancing side. In the case of rotors with negative lift near the tip, like the UH-60A, the trailed vorticity moves inboard in the azimuths of negative lift and creates a secondary lift impulse on the following blade at the junction of the first and second quadrant. This impulse is a significant source of vibratory harmonics. The state-of-the-art in airloads and structural loads predicted using coupled CFD/Comprehensive Analysis are also well benchmarked. [15]

The intent in this paper is to focus on predictions using the time-spectral method in CFD. The method has been applied to this rotor, at three different flight conditions, using uncoupled, CFD only simulations. The deformations prescribed were from the previous studies.[4] Coupled simulations for airloads have also been

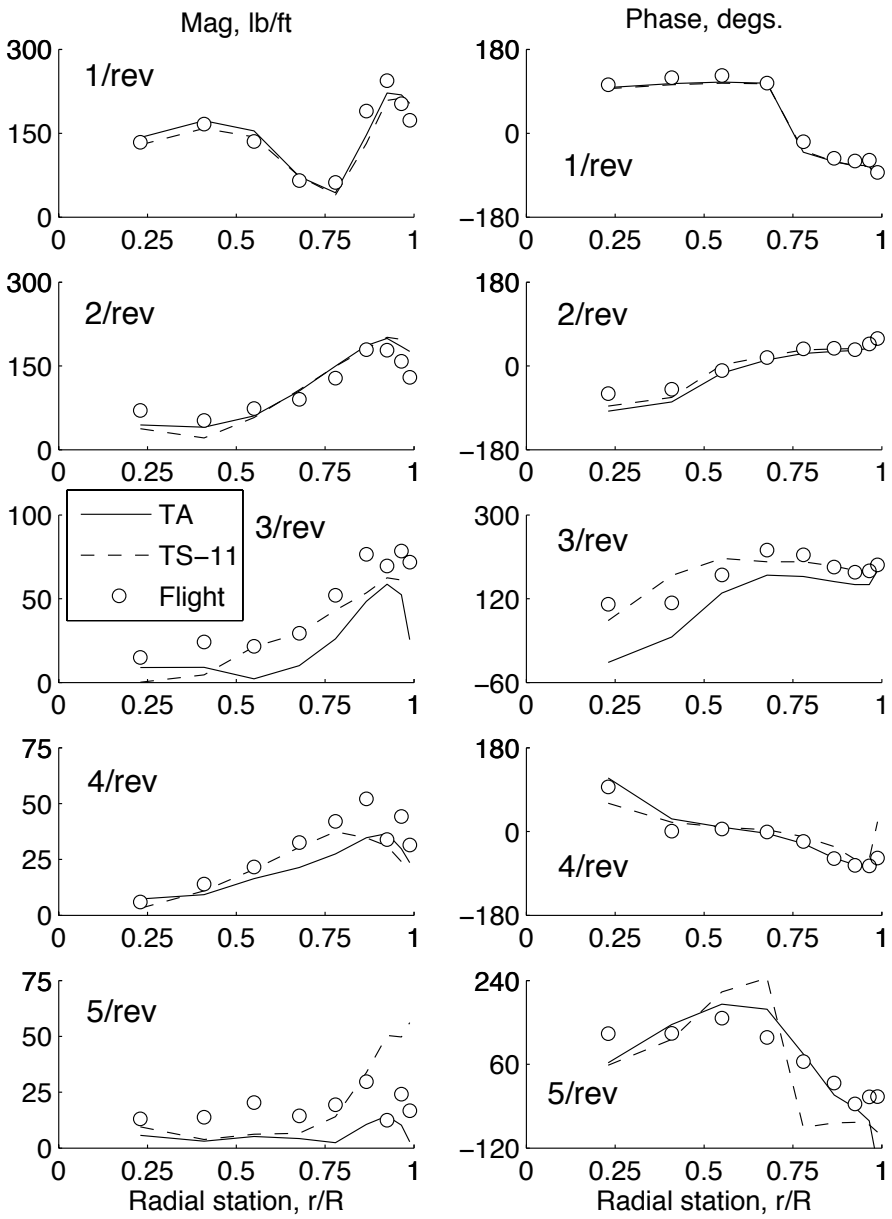

Figure 15. Normal force harmonics (1–5/rev) in magnitude and phase varying over blade span

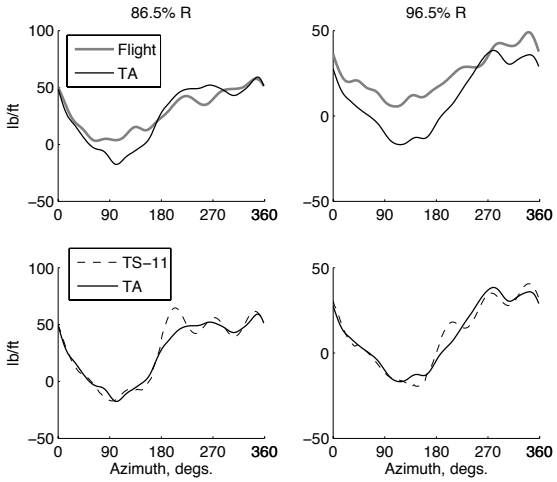

Figure 16. Measured and predicted chord forces for the UH-60A in high speed flight C8534

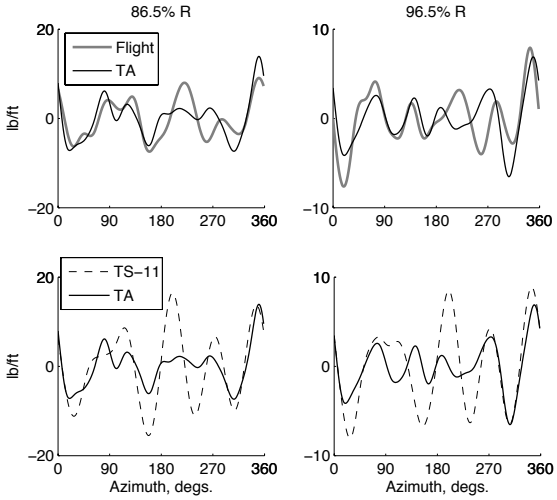

Figure 17. Measured and predicted vibratory chord forces (3-20 /rev) for the UH-60A in high speed flight C8534

carried out recently for three flights.[5] In this paper we focus only on the high speed flight, and investigate both airloads and structural loads in detail.

In the following subsections we present the results from both coupling methods – conventional and exact. Although both time-accurate and time-spectral computations were coupled with two procedures, our main discussion is focused on the results using time-spectral method and the results coupled with time-accurate computation are used for validation purpose. The time-spectral method is first studied using conventional coupling along with comparison with time-accurate computation, and the results are mostly discussed on airloads. The conventional coupling is then replaced with exact coupling, and both time-accurate and time-spectral methods are studied using exact coupling. The results from exact coupling procedure are focused on structural loads. Convergence pattern of both coupling procedures is also compared.

A. Computational Specifics

A total of 11 time instances were used for the time spectral computations. A structured mesh with 536 blocks and about 17 million nodes was employed. Both time-spectral and time-accurate computations were performed at the IBM cluster P4+ system at NAVO OCEANO MSRC (Naval Oceanographic Office Major Shared Resource Center). A total of 128 to 384 processors were used for our computations with 2GB memory per processor.

B. Time-Spectral with Conventional CFD/CA Coupling

The predicted normal forces at two blade sections are shown in Fig. 13. The figures at the top validate the time-accurate results with test data. The figures at the bottom compare the time-spectral results. Note that both are fully coupled first principle results. The trim conditions are identical but the deformations are different. The time-accurate results are similar to the benchmarked results at all radial stations, but we focus our attention on the outboard stations. This is because the largest errors are expected at these stations from the earlier study presented in Fig. 4. These are also the key stations for structural loads inboard. As shown earlier in Fig. 4, about 10% error is expected from aliasing with 11 time instances. Although the error pattern in Fig. 4 is valid when using uncoupled prescribed deformation, similar pattern (accumulated error) is expected for CFD/CA coupling procedure, and the effects are visible in Fig. 13. The impact of these errors on the vibratory harmonics is shown in Fig. 14. Note that for 11 time instances the cut-off frequency is $(11-1)/2 = 5$/rev. Thus a 6/rev content in the underlying waveform (time-accurate) will fold on to 5/rev, 7/rev to 4/rev, 8/rev to 3/rev and so on. Thus the vibratory harmonics 3,4, and 5/rev are influenced by 8,7, and 6/rev respectively. The radial distribution of the harmonics are shown in detail

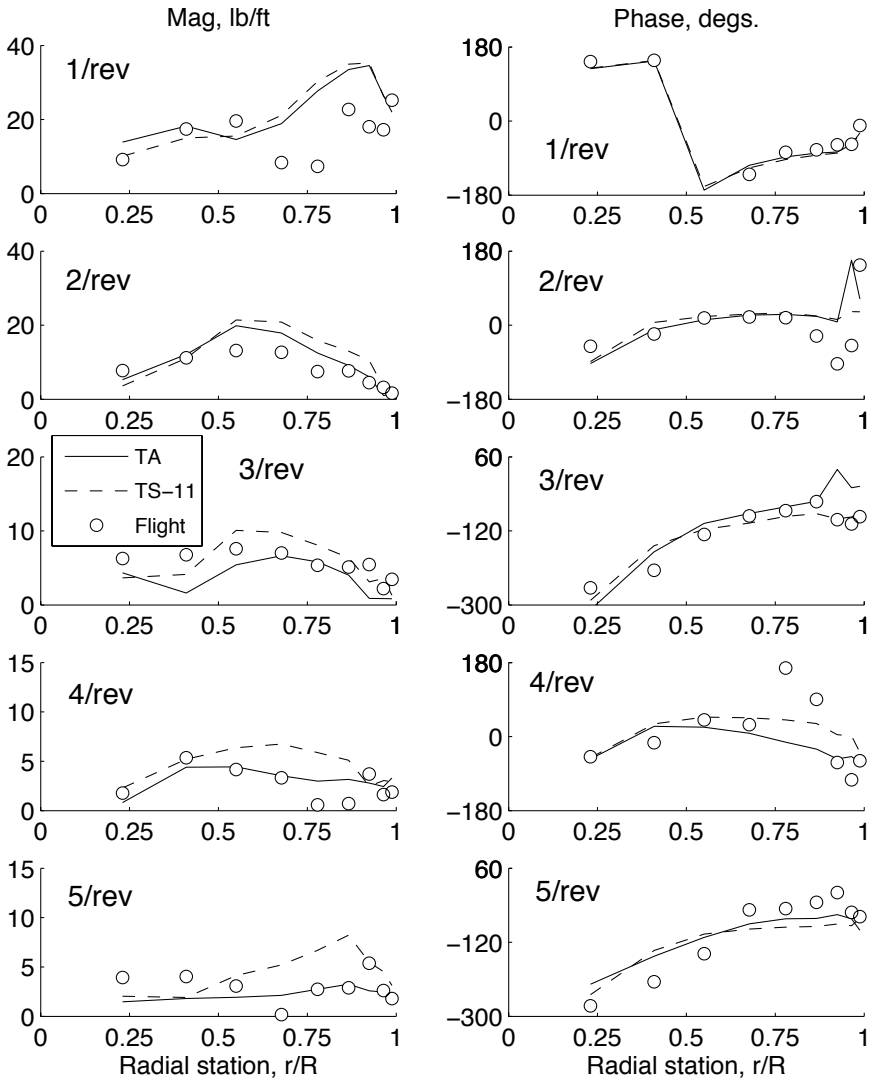

Figure 18. Chord force harmonics (1–5/rev) in magnitude and phase varying over blade span

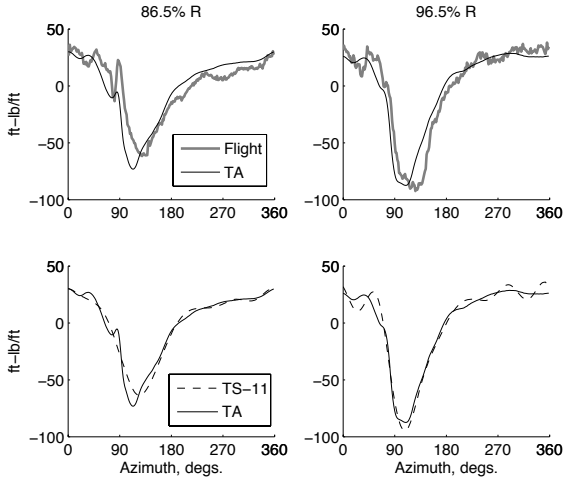

Figure 19. Measured and predicted pitching-moments (about 1/4-chord) for the UH-60A in high speed flight C8534

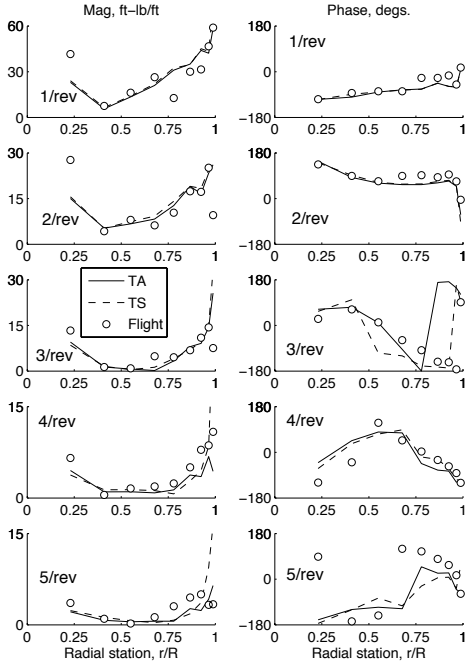

Figure 20. Pitching-moment harmonics (1–5/rev) in magnitude and phase varying over blade span

in Fig. 15. The 1/rev phase shows that the trim conditions are identical between the two methods. As 1 and 2/rev (and the steady) are in general in good agreement, 11 time instances appear to be reliable for performance calculations. At least for this flight condition, there is no significant aliasing from 11, 10, and 9/rev. The vibratory harmonics, however, are not satisfactory. The largest error occurs in 5/rev. The errors in 3 and 4/rev are relatively lower. This results in a somewhat acceptable structural load (shown later) as the first flap bending frequency lies between 3 and 4/rev (3.28/rev). We note, however, that the errors always over-predict by definition and thus always provides conservative loads estimates for design.

The predicted chord forces are shown in the same format in Figs. 16, 17, and 18. Compared to normal force, the penalty paid due to aliasing errors in chord-forces are more severe on the lead-lag dynamics. The first chord bending frequency sits between 4 and 5/rev for this rotor (4.66/rev). The aliasing errors at this harmonics will now have a significant impact on vibratory structural loads (shown later). The typical prediction in chord loads is unsatisfactory in itself, but that study is beyond the scope of the present paper. Here, we focus on the comparison between time-accurate and time-spectral results. The chord forces are in general very well predicted by the time-accurate analysis of the present study – both in phase and magnitude, see Figs. 16 and 17, except for the 1/rev magnitude. For time-spectral predictions, the aliasing errors follow the same trend as normal forces – largest in 5/rev (more than 100%) followed by 4 and 5/rev. The errors in 4 and 5/rev are visible in the waveform of the vibratory harmonics shown in Fig. 17. The effect of this error on structural load is seen later in 5/rev chord bending moment.

The pitching moments drive the key vibratory loads mechanism (large elastic twist deformation) in this flight. The predicted pitching moments are studied in Figs. 19 and 20. Figure 19 validates the time-accurate pitching moments. The three-dimensional, unsteady, transonic tip relief effect that generates the impulsive wave form in the first quadrant is well predicted by both time-accurate and time-spectral method. The effect of this mechanism is mainly on the 1 and 2/rev pitching moments and therefore, as expected, there is little aliasing error in the waveform. The harmonic break-down of the pitching moment distribution over span is given in Fig. 20. The spectrum of the time-accurate pitching moment waveform is more band-limited compared to the sectional forces and hence there is little error even in the vibratory harmonics. Note that the large over-prediction of 4, and 5/rev is not a direct effect of aliasing error but an artifact of the grid.

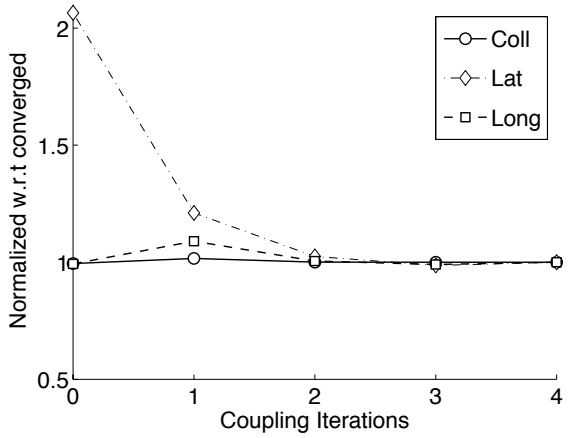

Figure 21. Convergence of CFD/CA conventional coupling; Time-spectral method; UH-60A in high speed flight C8534

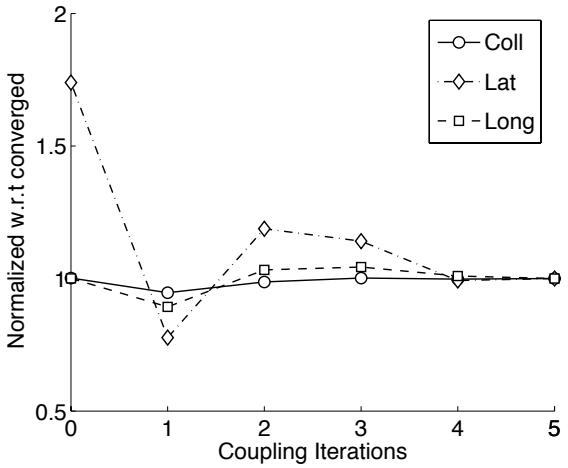

Figure 22. Convergence of CFD/CA exact coupling; Time-spectral method; UH-60A in high speed flight C8534

	θ_{75}	θ_{1c}	θ_{1s}	C_Q/σ
flight test	14.0	4.85	-10.6	0.00909
time-accurate	14.6	1.6	-8.9	0.00841
time-spectral	14.8	1.76	-9.1	0.00864
basic UMARC	14.8	3.07	-9.1	0.00939

Figure 23. Predicted trim angles and main rotor shaft power using exact CFD coupling

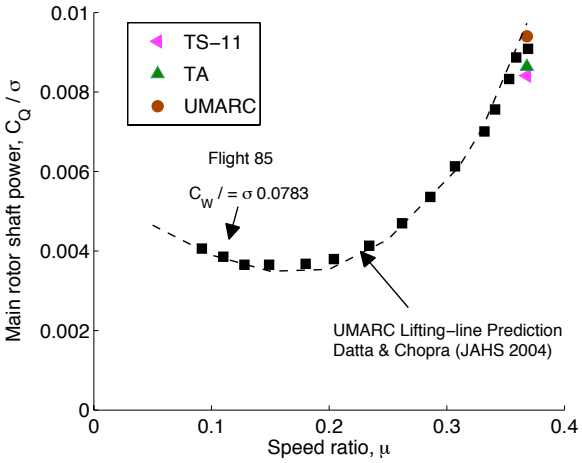

Figure 24. Predicted main rotor shaft power varying with forward speed; flight C8534 results plotted as symbols; Lifting-line predictions from Ref.[23]

The time-accurate waveform shows higher harmonic oscillations near the tip caps and these fold on to the spectral predictions at the lower harmonics.

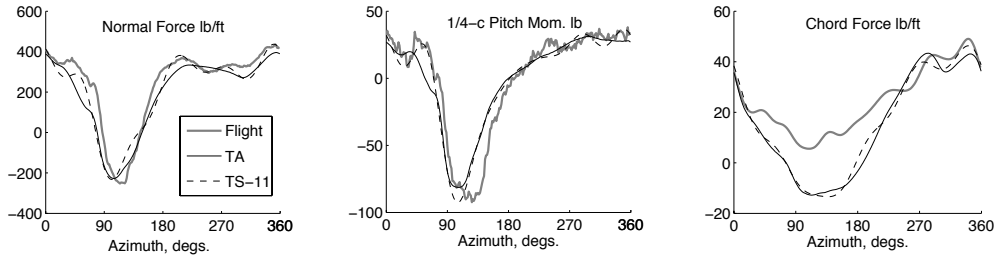

Figure 25. Predicted airloads using exact fluid-structure interface and modified *delta* procedure: time-accurate and time-spectral methods in CFD; UH-60A in high speed flight C8534

C. Time-Spectral with Exact CFD/CA Coupling

The time-accurate and time-spectral calculations are now re-performed with the exact interface and the modified delta coupling procedure. The convergence of the modified delta procedure, and the converged airload predictions are similar to the conventional coupling but not identical. The convergence patterns of conventional and exact coupling are shown in Figs. 21 and 22. Both results are from time-spectral computation in CFD. The converged trim angles and rotor shaft power are compared with flight test data in Table 23.

The pattern of time-accurate and time-spectral predictions remain the same, as expected, and is shown in Fig. 25. The focus in this section is on structural loads. First, the structural loads obtained using conventional and exact coupling procedures are compared in Figs. 26 and 27. The time-accurate predictions are used for both procedures and, the purpose of this comparison is the validation of the exact coupling procedure. Once validated, the procedure is then used to compute time-accurate and time-spectral structural loads in Figs. 28 and 29.

Note that the exact coupling procedure is targeted for unstructured grids and advanced geometry blades. It is expected to provide a very close comparison in the present case. The structured grids, the relatively conventional blade shape, and the use of all spanwise grid points in the conventional interface enables the validation of the exact method. This is because, as shown earlier, the dominant terms of the exact interface reduces to a conventional interface (of sectional airloads) in the limit of refinement on a structured grid with the sections defined as per the underlying structural model.

Figure 26 shows that the flap bending moments are identical between the two coupling methods – conventional and exact. The calculations are using time-accurate method in CFD and the validation is identical to the present state-of-the-art. Figure 27 shows the torsion loads. Again, there is no phenomenological difference between the two predictions. The state-of-the-art discrepancy in 4/rev predictions, manifest in the retreating side (near 270° azimuth), remain. The waveform on the retreating side in the outboard sections of the blade, 50% and 90% (similar to 50%, not shown), however, are different. The exact predictions appear to have an improved waveform. This stems from an improved 3/rev harmonic component. Note that predictions using measured airloads have a similar waveform in the retreating side as the conventional coupling result. This is consistent, as the measured airloads were also imposed as sectional airloads, not directly as surface pressures with an exact interface. The effect of the improved 3/rev and the remaining 4/rev discrepancy is reflected in the pitch link load harmonics.

Figure 28 shows the bending moments from time-spectral calculations. The error in 3/rev normal force shown earlier in Fig. 15 leads to a reduced peak magnitude in the flap bending moments. The error in 5/rev chord force is evident in the chord bending moments. The torsion loads, shown in Fig. 29, are very similar, consistent with the airload trends shown earlier in Fig. 20. The pitch link load harmonics are almost identical. The 6/rev and higher harmonics in spectral are entirely from aliasing errors.

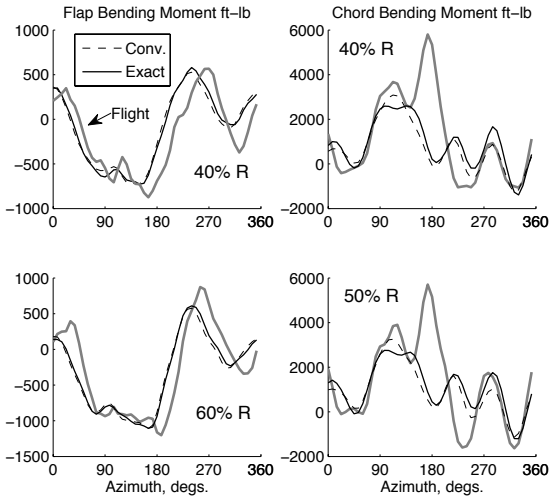

Figure 26. Predicted flap and chord bending moments compared using conventional and exact coupling procedures; Time-accurate method in CFD; UH-60A in high speed flight C8534

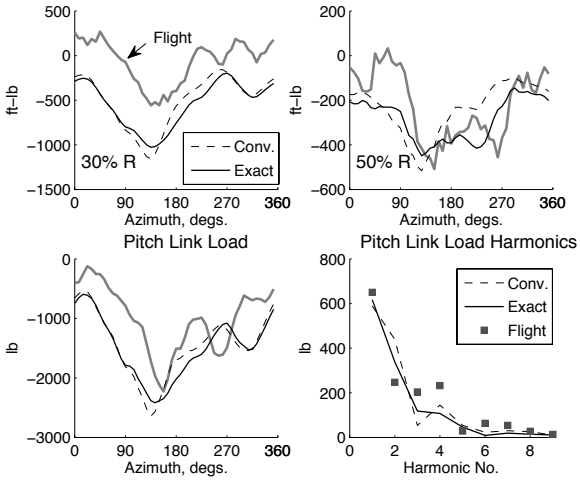

Figure 27. Predicted torsion moment and Pitch link loads compared between conventional and exact coupling procedures; Time-accurate method in CFD; UH-60A in high speed flight C8534

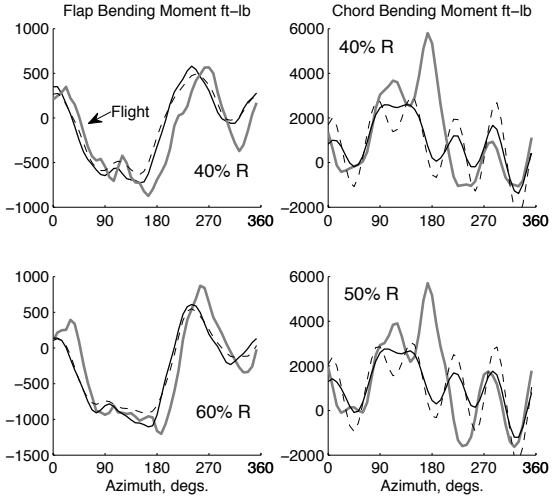

Figure 28. Predicted flap and chord bending moments compared using time-accurate and spectral methods in CFD; Exact CFD/CA coupling procedure; UH-60A in high speed flight C8534

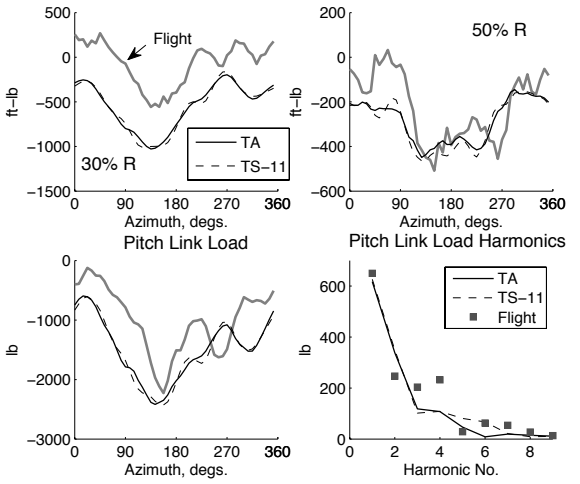

Figure 29. Predicted torsion moments and pitch link loads compared using time-accurate and spectral methods in CFD; Exact CFD/CA coupling procedure; UH-60A in high speed flight C8534

V. Conclusions and Future Work

A Fourier collocation based time-spectral method was used to accurately compute periodic helicopter rotor flows in steady level flight. The primary objective was to study accuracy and convergence patterns of this method for rotor flows by quantifying the associated error terms (aliasing errors). The vibratory airloads and structural loads of the UH-60A rotor were predicted using time-spectral method based CFD/Comprehensive Analysis coupling. The predictions were validated with flight test data from a high vibration flight of this helicopter. The time-accurate and time-spectral methods were compared consistently at the same trim condition. The CFD/Comprehensive Analysis coupling procedure was different from existing methods, and an exact fluid-structure interface was implemented in this paper. A modified delta coupling procedure was proposed that preserves the exactness of the interface. Both time-accurate and time-spectral analysis were carried out using the exact coupling procedure. The followings are the conclusions of this study.

1. The time-spectral method for a four-bladed helicopter requires at least 11 time-instances for the prediction of vibratory harmonics. The cut-off frequency for this case is 5/rev, and the vibratory harmonics (3,4,5)/rev contain folding frequency errors from (6,7,8)/rev of the underlying waveform. The harmonic error is less than 5% in pitching moments, approximately 5–10% in vibratory normal force, and 10–20% in vibratory chord force. The resulting error in vibratory structural load is unsatisfactory - primarily because the flap and chord bending frequencies of this rotor (3.28/rev and 4.66/rev) lie within the range of alias frequencies.

2. For this rotor, and for the flight condition studied, the errors decay asymptotically following theoretical trends for smooth functions. Convergence depends on the spectrum of the underlying waveform but is quantifiable. A total of 17 time-instances decay the error to 1% the level of time-accurate predictions, while a total of 25 time-instances decay the error to 0.1%.

3. It is concluded that without any anti-aliasing filter, reliable prediction of structural loads require as many time-instances as, at least, 4 times the blade number. It also appears, that reliable prediction of performance require, at least, 2 times the blade number.

4. The saving in computational time with respect to time-accurate simulations is substantial – approximately one-fifth the time with 11 time instances, one-third with 17 time-instances and one-half for 25 time instances.

5. The fluid-structure interface implemented in this study, along with the modified delta method, provides a generic delta coupling capability in rotary-wing CFD/CSD for unstructured grids, advanced geometry blades, and generic structural models.

In summary, the time-spectral method in CFD appears to be an effective procedure for the calculation of rotor vibratory loads. The method can be particularly attractive if equipped with anti-aliasing filters. The method also opens opportunity for blade shape optimization as the steady-state formulation of the fluid equations allow the use of adjoint based methods – similar to the gradient based optimization procedures long used in the structural domain. Thus the method has significant potential for design optimization using coupled CFD/CSD and VFD procedures.

References

[1]Canuto, C., Hussaini, M. Y., Quarteroni, A., and Jr. Zang, T. A., T. A., Jr. Zang "Spectral Methods in Fluid Dynamics," *Springer,* 1998.

[2]Van der Weide, E., Gopinath, A., and Jameson, A., "Turbomachinery applications with the time spectral method," *AIAA Paper 05-4905*, Toronto, Canada, Jun. 2005.

[3]Sankaran, S., Gopinath, A., Van der Wedie, E., Kim, S., Tomlin, C., and Jameson, A., "Aerodynamics and Flight Control of Flapping Wing Flight Vehicles: A Preliminary Computational Study," *AIAA Paper 05-0841*, Reno, NV, Jan. 2005.

[4]Choi, S., Alonso, J. J., Van der Weide, E., and Sitaraman, J., "Validation Study of Aerodynamic Analysis Tools for Design Optimization of Helicopter Rotors," *AIAA Paper 07-3929*, Miami FL., June 2007.

[5]Choi, S., and Datta, A., "Time-Spectral Method for the CFD Prediction of Main Rotor Vibratory Loads," *5th International Conference on CFD*, Seoul, Korea, July. 2008.

[6]Choi, S., Lee, K., Alonso, J. J., and Datta, A., "Study on Time-Spectral and Adjoint-Based Design Optimization of Helicopter Rotors," *AHS Specialist's Conference on Aeromechanics*, San Francisco CA., Jan. 2008.

[7]Hesthaven, J., Gottlieb, S., and Gottlieb, D., "Spectral Methods for Time-Dependent Problems," *Cambridge Monographs on Applied and Computational Mathematics,* 2007.

[8]Gopinath, A., "Efficient Fourier-Based Algorithms for Time-Periodic Unsteady Problems," *Ph.D thesis, Stanford University*, Apr. 2007.

[9]Reuther, J. J., Jameson, A., Alonso, J. J., Rimlinger, M., and Saunders, D., " Constrained multipoint aerodynamic shape optimization using an adjoint forumlation and parallel computers: Part I & II," *Journal of Aircraft, 36(1):51-74*,1999

[10]Jameson, A., "Aerodynamic design via control theory ," *Journal of Scientific Computing, 3:233-260*,1988

[11]Mani, K., and Mavriplis, D. J., "An Unsteady Discrete Adjoint Formulation for Two-Dimensional Flow Problems with Deforming Meshes," *AIAA 45th Aerospace Science Meetings & Exhibit,*Reno, NV, Jan. 2007.

[12]Nadarajah, S., McMullen, M., and Jameson, A., "Optimal control of unsteady flows using time accurate and non-linear frequency domain methods," *AIAA Paper 2003-3875*,Orlando, FL, Jun. 2003.

[13]M.S.McMullen, A. Jameson, and J.J.Alonso, "The Application of Non-Linear Frequency Domain Methods to the Euler and Navier-Stokes Equations," *Ph.D dissertation*,Stanford University, Mar. 2003.

[14]Thomas, J. P., Dowell, E. H., and Hall, K. C., "Modeling three-dimensional inviscid transonic limit cycle oscillation using a harmonic balance approach," *ASME International Mechanical Enginnering Conference and Exposition*,New Orleans, 2002.

[15]Datta, A., Nixon, M. and Chopra, I., "Review of Rotor Loads Prediction with the Emergence of Rotorcraft CFD," *Journal of the American Helicopter Society*, Vol. 52, (4), October 2007, pp. 287–217.

[16]Tung, C., Cardonna, F.X., and Johnson, W.R., "The Prediction of Transonic Flows on an Advancing Rotor," *Journal of the American Helicopter Society*, Vol. 31, (3), July 1986, pp. 4–9.

[17]Datta, A. and Chopra, I., "Validation and Understanding of UH-60A Vibratory Loads in Steady Level Flight," *Journal of the American Helicopter Society*, Vol. 49, (3), July 2004, pp 271-287.

[18]Datta, A., and Chopra, I, "Validation of Structural and Aerodynamic Modeling using UH-60A Airloads Program Data," *Journal of the American Helicopter Society*, Vol. 51, (1), January 2006, pp. 43–58.

[19]Datta, A., Sitaraman, J., Chopra., I, and Baeder, J., "CFD/CSD prediction of rotor vibratory loads in high speed flight," in press, *Journal of Aircraft*, Vol. 43, (6), Nov.-Dec. 2006, pp. 1698–1709.

[20]Datta, A. and Chopra, I., "Prediction of UH-60 Main Rotor Structural Loads using CFD/Comprehensive Analysis Coupling," 32nd European Rotorcraft Forum, Maastricht, The Netherlands, September 12–14, 2006; in press for *Journal of the Americal Helicopter Society*, October, 2008.

[21]Maman, N. and Farhat, C., "Matching Fluid and Structure Meshes for Aeroelastic Computations: A Parallel Approach," *Computers and Structures*, Vol. 54, (4), 1995, pp. 779–785.

[22]Cebral, J. R., and Lohner, R., "Conservative Load Projection and Tracking for Fluid-Structure Problems," *AIAA Journal*, Vol. 35, (4), 1997, pp. 687–692.

[23]Farhat, C., Lesoinne, M. and LeTallec, P., "Load and Motion Transfer Algorithms for Fluid/Structure Interaction Problems with Non-matching Discrete Interfaces: Momentum and Energy Conservation, Optimal Discretization and Application to Aeroelasticity," *Computer Methods in Applied Mechanics and Engineering*, Vol. 157, (1), April 1998, pp. 95–114.

[24]Slone, A. K., Pericleous, K., Bailey, C. and Cross, M., "Dynamic Fluid-Structure Interaction Using Finite Volume Unstructured Mesh Procedures," *Computers and Structures*, Vol. 80, (5), March 2002, pp. 371–390.

[25]Michler, C., Van Brummelen, E. H., Hulshoff, S. J. and De Borst, R., "The Relevance of Conservation for Stability and Accuracy of Numerical Methods for Fluid-Structure Interaction," *Computer Methods in Applied Mechanics and Engineering*, Vol. 192, (37), September 2003, pp. 4195–4215.

[26]Hodges, D. H., and Dowell, E. H., "Nonlinear Equations of Motion for the Elastic Bending and Torsion of Twisted Nonuniform Rotor Blades," NASA TN D-7818, December 1974.

[27]Kvaternik, Raymond G., Kaza, Krishna R. V., Nonlinear Curvature Expressions for Combined Flapwise Bending, Chordwise Bending, Torsion, and Extension of Twisted Rotor Blades, NASA TM X-73, 997, 1976.

[28]Ormiston, R. A., Hodges, D. H., and Peters, D. A., "On the Nonlinear Deformation Geometry of Euler-Bernoulli Beams," NASA Technical Paper 1566, 1980.